

Transitions between drift waves in a magnetized cylindrical plasma: experiments and fluid model, solved with a spectral method

Etienne Gravier^{1,a}, Emmanuel Plaut², Xavier Caron¹, and Mathieu Jenny²

¹ Institut Jean Lamour, UMR 7198 CNRS, Université de Lorraine, Bd des Aiguillettes, 54506 Vandœuvre-lès-Nancy Cedex, France

² LEMTA, UMR 7563 CNRS, Université de Lorraine, 2 av. de la Forêt de Haye, 54516 Vandœuvre-lès-Nancy Cedex, France

Received 16 October 2012 / Received in final form 21 November 2012

Published online 24 January 2013 – © EDP Sciences, Società Italiana di Fisica, Springer-Verlag 2013

Abstract. A bifurcation scenario between collisional drift waves with different azimuthal wavenumbers m in a magnetized plasma column is experimentally studied, and compared with a linear two-fluid model solved with a new spectral method. The control parameter is the potential of an internal metallic tube in the experiments, the electron drift along the axis of the cylinder in the model. By increasing this parameter, we find bifurcations from azimuthal modes $m = 5$ to $m = 1$. The linear properties of the model agree well with the experimental observations.

1 Introduction

Small scale cylindrical devices, together with numerical simulations, can play an important role in understanding basic plasma processes. It is now widely believed that low-frequency turbulence developing from micro instabilities is responsible for the phenomenon of anomalous transport. This issue is related to the problem of anomalous transport in magnetically confined fusion plasmas [1,2].

Low-frequency density fluctuations are easily observed in cylindrical magnetized plasma columns. These cylindrical machines are of fundamental interest and can provide a testing ground for comparisons of numerical simulations with experiments. In particular, different plasma experiments exhibiting drift wave instabilities have been published, in Q-machines [3,4], Mirabelle [5,6], Mistral [7], Kiwi [8], Alexis [9,10], or Columbia [11,12] to name only a few. These experiments show regular, chaotic or turbulent regimes.

Here we focus on the Mirabelle device [5]. Our study shows a clear bifurcation scenario between regular waves in a magnetized plasma column. These waves are collisional drift waves induced by a steady-state pressure gradient in the direction transverse to the magnetic field. Bifurcation scenarios can be obtained by using the high sensitivity of an influent parameter. The typical observation is that the azimuthal wavenumber m of the wave strongly depends on this control parameter. The potential of an inner insulated tube acts as the control parameter of the dynamical regimes of drift waves.

We also report on a comparison of the experimental results to the linear properties of a two-fluid model. In this

model, the control parameter is the axial electron drift in the base state. In order to solve this model, a new, efficient spectral method inspired from fluid dynamics studies [13] is developed. This also yields a better understanding of the mathematical conditions that have to be fulfilled on the axis of the machine, as it will be discussed in Section 3.3. From a physical point of view, the influence of an axial electron drift on plasma instabilities is an important general topic in plasma physics, which has for instance been studied in Q-1 [4] or in Alexis [10].

The article is organized as follows. The experimental setup is described with the measurement techniques in Section 2.1. A scenario involving five modes as function of the potential of the inner insulated tube is reported in Section 2.2. In Section 3, a study of a linearized two-fluid model is performed, considering Gaussian and non-Gaussian density profiles. The first case is considered as a simple reference, the latter more realistic case requires a numerical solution: here the new spectral method is presented. Numerical results are compared to experimental results. In the concluding Section 4, we discuss the link between the experimental and theoretical control parameters, and propose some future prospects.

2 Experimental study

2.1 Experimental setup and diagnostics

The experiments were conducted in the cylindrical MIRABELLE device [5]. The device is made of two large multipolar plasma chambers connected to each end of a stainless steel vacuum vessel. This vessel is immersed in

^a e-mail: etienne.gravier@ijl.nancy-universite.fr

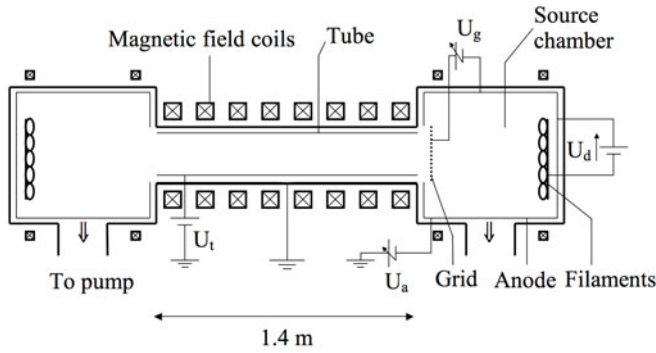


Fig. 1. Sketch of the MIRABELLE experiment.

a set of coils to generate a homogeneous magnetic field up to 120 mT along the axis of the cylinder (Fig. 1). A metallic tube of radius $a = 11.5$ cm is inserted inside the vessel. At the one end of the device, an Argon plasma is produced using a standard thermionic discharge. The cathode consists of 24 equally spaced tungsten filaments (biasing U_d with respect to the anode) located on a vertical plane at the end of the source chamber. The biasing of the anode with respect to the ground is U_a . A high transparency stainless grid is located between the source chamber and the plasma column. It controls the energy and the flux of the electrons flowing from the source chamber into the plasma column. The biasing U_g of this grid influences the axial drift of the electrons along the plasma column. Moreover, the biasing of the insulated internal metallic tube (potential U_t in Fig. 1) also influences the axial drift of the electrons. This biasing is the dynamical control parameter chosen for the experiments. The working pressure in Argon gas is typically $p = 10^{-4}$ Torr. For the other typical parameters the reader can refer to [14].

Plasma parameters are measured with Langmuir probes. First a three-dimensional movable probe installed inside the plasma column is used for the measurement of the radial profiles. This probe used with a second probe as phase reference also permits the measurement of the parallel wavelength λ_z of drift waves.

Moreover, an azimuthal array of 32 Langmuir probes (0.5 mm in diameter, 4 mm in length) is used for the measurement of poloidal mode structures. This set-up is connected to two VXI plug-in units for the synchronous acquisition of the time-series. The sampling rate is 200 kHz with 16 bits of resolution. This fast acquisition system allows a real-time imaging of the spatiotemporal regime of the system and the integer number m characterizing a regular azimuthal mode can be determined.

2.2 Experimental scenario

The mean radial profiles of the density (Fig. 2) have been recorded with $U_g = 8$ V, $U_a = 0$ V, and $U_d = 50$ V. The experimental control parameter is the polarization of the tube U_t , which is varied from 0 to 4.2 V by steps $\delta U_t = 0.2$ V, from 4.2 to 9 V by steps $\delta U_t = 0.4$ V. From other similar experiments [14], we expect that the

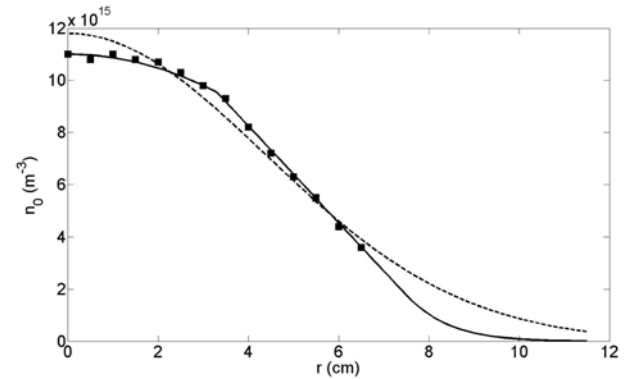


Fig. 2. Experimental (squares), Gaussian (dotted line) and interpolated (solid line) mean density profiles in the MIRABELLE experiment at $p = 10^{-4}$ Torr. The error bars are not displayed because they are of the order of the size of the squares [14]. For the Gaussian profile, see Section 3.2, and for interpolated profile, see Section 3.4.

mean plasma potential profile is uniform excepted in the sheath, within ± 0.4 V, so that global electric rotation drift effects are small. We also expect that, when U_t increases, the mean value U_p of the plasma potential increases, whereas the mean density profile is not altered. Collisional drift waves instabilities are observed [14], and characterized from spatiotemporal data such as the ones of Figure 3. From such measurements one can extract the frequency $\omega_r/2\pi$ of the wave, and its azimuthal wavenumber m . When U_t increases, the wavenumber m decreases, as shown in Figure 4. Meanwhile, for a mode m the frequency increases, until the mode suddenly changes for a lower mode with a lower frequency. In Figure 5 the frequencies are plotted versus the observed azimuthal wavenumber m . Low mode frequencies depend linearly on m whereas for $m = 4$ and $m = 5$ the frequency reaches a plateau.

Similar modes have been obtained in the KIWI experiment [15,16] or in our MIRABELLE device [6]. But the study of the frequency as a function of the bias of the tube or as a function of the mode number has never been performed before in the range $m = 1$ to $m = 5$. It is also important to mention that high modes have been studied in the VINETA device [17] for a cylindrical helicon plasma in which electron-ion collisions play a very important role in the behavior of drift waves instabilities. In the MIRABELLE experiment, the electron-ion collisional rate is negligible.

3 Linear study of a two-fluid model

3.1 Base state and linear problem

The equations of the model are the two-fluid equations for a weakly ionized plasma with cold ions given by Self [18] or Ellis et al. [19,20]. Collisions with neutrals are dominant for both electrons and ions and are characterized by the collision frequencies ν_e and ν_i , respectively. The

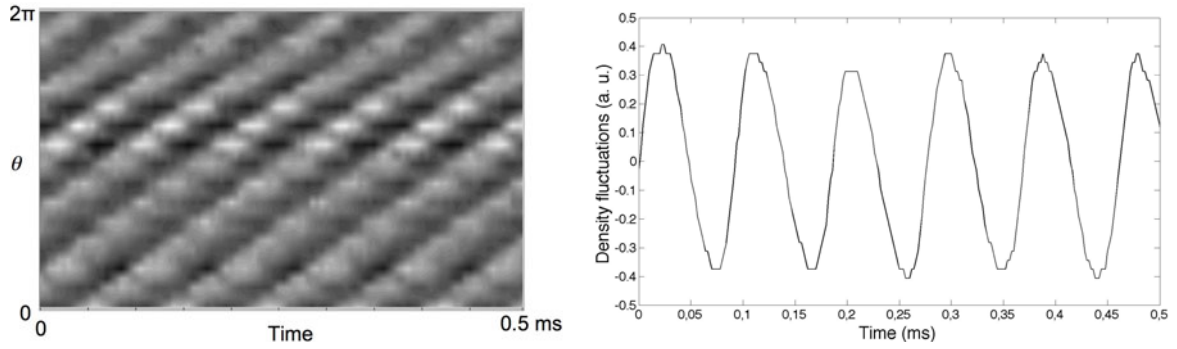


Fig. 3. Spatiotemporal data for $U_t = 0$ V, $m = 5$. The floating potential, recorded at $r = 7$ cm, is plotted versus time and θ , the azimuthal angle (left). A one probe signal of the density fluctuations is also recorded and plotted versus time (right).

basic density profile n_0 is assumed to depend only on the radial coordinate r . Indeed, experimentally there is no difference observed between the mean profiles measured by two Langmuir probes separated by an axial distance equal to 0.5 m. The existence of a radial density gradient dn_0/dr induces an azimuthal electron diamagnetic drift,

$$\mathbf{v}_d = -\frac{KT_e}{eB}\kappa_n\hat{\theta}, \quad (1)$$

with K the Boltzmann constant, T_e the electron temperature,

$$\kappa_n = \frac{1}{n_0} \frac{dn_0}{dr} \quad (2)$$

and e the absolute value of the electron charge. This drift is a source of free-energy that can lead to the growth of the fluctuations. Moreover, we assume like in [19,20] that, in the base state, electrons drift parallel to the magnetic field at speed u_0 . Recent observations of the modification of drift instabilities by plasma flows parallel to the magnetic field have been shown [10]. This drift is the control parameter of our model. We assume that it is linked (i.e., roughly proportional) to the tube potential U_t , and plays a similar role, as will be discussed in the conclusion.

All frequencies are assumed to be small when compared to the ion cyclotron frequency $\Omega_c = eB/m_i$, with m_i the ion mass.

Linear perturbations are assumed. For example the electrostatic potential of a wave is assumed to be of the form

$$\Phi(r, \theta, z, t) = \phi(r) \exp [i(m\theta + k_{\parallel}z - \omega t)] + c.c. \quad (3)$$

After linearization, the two-fluid model yields a set of coupled equations, e.g. equations (4) to (8) of [20]. Note that in equation (7) of [20] there misses a term $-e\tilde{n}B(\mathbf{v}_d \times \hat{z})$ in the right hand side. After some algebra, one can express all perturbation fields in terms of the potential $\phi(r)$, and obtain a differential equation for $\phi(r)$,

$$\frac{d^2\phi}{dr^2} + \left(\kappa_n + \frac{1}{r}\right) \frac{d\phi}{dr} + \left(Q(r) - \frac{m^2}{r^2}\right) \phi = 0, \quad (4)$$

with

$$Q(r) = \frac{1}{(\omega + i\nu_i)\rho_s^2} \left(\omega^* - \frac{\omega^* + i\nu_{\parallel}\omega}{\omega - \omega_{\parallel} + i\nu_{\parallel}} \right), \quad (5)$$

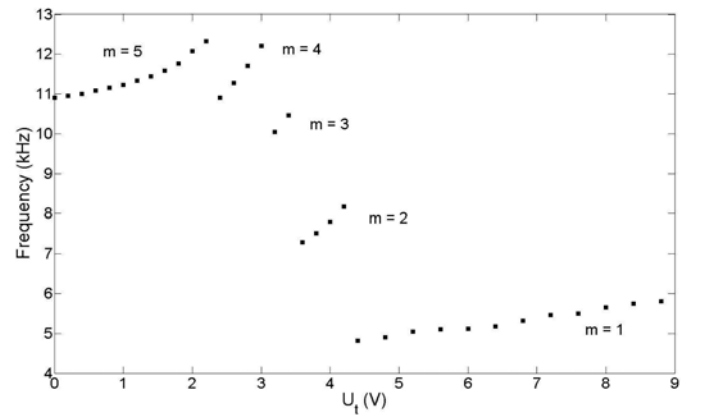


Fig. 4. Experimental bifurcation scenario: frequencies $\omega_r/2\pi$ of the drift waves vs. U_t . The azimuthal wavenumber is indicated.

and

$$\omega^* = \frac{m}{r} v_d = -\frac{m}{r} \frac{KT_e}{eB} \kappa_n \quad (6)$$

the electron diamagnetic frequency,

$$\nu_{\parallel} = \frac{k_{\parallel}^2 KT_e}{m_e \nu_e}, \quad \omega_{\parallel} = k_{\parallel} u_0, \quad (7)$$

$c_s = \sqrt{\frac{KT_e}{m_i}}$, $\rho_s^2 = \frac{c_s^2}{\Omega_c^2}$, m the azimuthal wavenumber, $k_{\parallel} = 2\pi/\lambda_z$ the axial wavenumber, ν_e (resp. ν_i) the electron-neutral (resp. ion-neutral) collision rates.

Equation (4) can also be written

$$L\phi = -Q(r)\phi \quad (8)$$

with

$$L\phi = \frac{d^2\phi}{dr^2} + \left(\frac{1}{r} + \kappa_n\right) \frac{d\phi}{dr} - \frac{m^2}{r^2} \phi. \quad (9)$$

It has to be solved with the boundary condition

$$\phi(a) = 0 \quad (10)$$

that expresses the isopotential nature of the tube.

The plasma parameters relevant for the MIRABELLE experiment, with an Argon plasma, are: $p = 10^{-4}$ Torr,

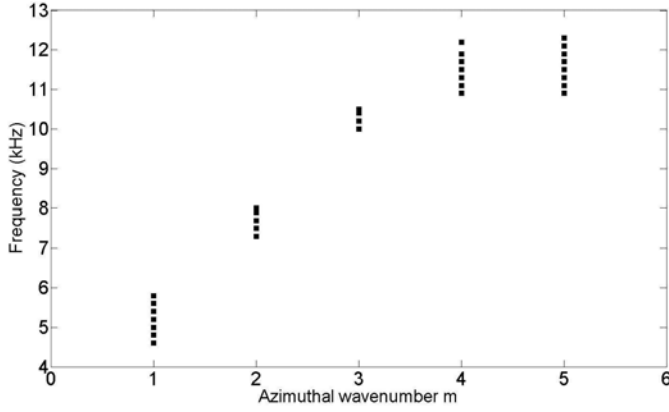


Fig. 5. Experimental bifurcation scenario: frequencies plotted against the azimuthal wavenumber m . The data are the same as in Figure 4. Two points are separated by $\delta U_t = 0.4$ V for $m = 1$ and $\delta U_t = 0.2$ V for other modes.

$T_e = 3$ eV, $B = 37$ mT, $a = 11.5$ cm. We have also set the axial wavenumber to its value measured in [14]:

$$k_{\parallel} = 2 \text{ m}^{-1}. \quad (11)$$

The collision frequencies are approximately $\nu_e = 1.0 \times 10^6 \text{ s}^{-1}$ [21] and $\nu_i = 750 \text{ s}^{-1}$ [22]. The uncertainties on the plasma parameters are assumed to be of the order of 0.2 eV for T_e [14], 50% for ν_e , 30% for B , 20% for k_{\parallel} . Sensitivity analyses will be performed.

3.2 Case of a Gaussian density profile: semi-analytical results

If the density profile is assumed to be Gaussian,

$$n_0(r) = N_0 \exp(-r^2/r_0^2), \quad (12)$$

with r_0 the Gaussian parameter, one has $\kappa_n = -2r/r_0^2$, hence ω^* and Q do not depend on r .

Therefore equation (8), together with the boundary condition (10), can be solved with a change of variables and an hypergeometric function, as shown by [23]. This yields the values of $Q = Q(m, a, r_0)$ or

$$b = b(m, a, r_0) = \rho_s^2 Q(m, a, r_0) = \frac{\rho_s^2}{a^2} S\left(m, \frac{r_0}{a}\right) \quad (13)$$

according to dimensional analysis. The functions S and b increase with m ; typical values are shown in Figure 2 of [20]. Once they are computed, ω can be calculated by inverting equation (5), i.e. by solving

$$b\omega^2 + \omega[(1+b)i\nu_{\parallel} + b(i\nu_i - \omega_{\parallel})] - \nu_{\parallel}(b\nu_i + i\omega^*) + \omega_{\parallel}(\omega^* - i\nu_i) = 0. \quad (14)$$

In the frequent case where ω , ω^* , ω_{\parallel} are small as compared to ν_{\parallel} , ν_i is very small as compared to ν_{\parallel} , one can show that

$$\omega_r = \text{Re}(\omega) = \omega_1 + \omega_2 \quad (15)$$

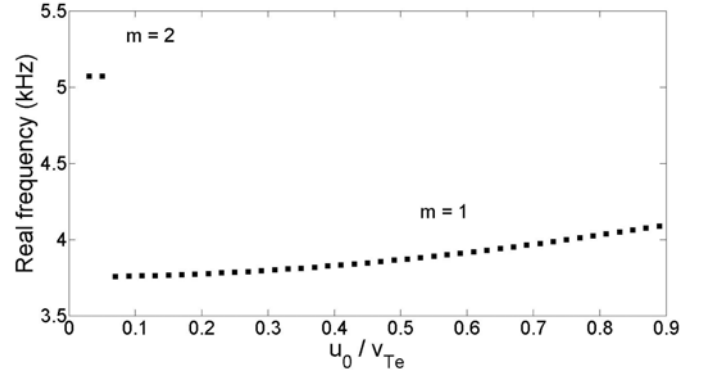


Fig. 6. Numerical real frequencies $\omega_r/2\pi$ of the fastest growing mode vs. the axial electron drift in the case of a Gaussian profile.

with the leading-order real frequency

$$\omega_1 = \frac{\omega^*}{1+b} = \frac{2m}{1+b} \frac{KT_e}{eBr_0^2} \quad (16)$$

and an higher-order correction

$$\omega_2 = \frac{b\omega_1(\omega_{\parallel} - 2\omega_1)(\omega_{\parallel} + b\omega_1)}{(1+b)^2\nu_{\parallel}^2} + \frac{b}{(1+b)^2} \frac{\nu_i}{\nu_{\parallel}} [\omega_{\parallel} + (b-1)\omega_1]. \quad (17)$$

Moreover one also obtains

$$\omega_i = \text{Im}(\omega) = \frac{\omega_1(\omega_{\parallel} + b\omega_1)}{(1+b)\nu_{\parallel}} - \frac{b}{1+b} \nu_i \quad (18)$$

which corresponds to a corrected version of equation (10) of [20]. This shows that electron-neutral collisions are destabilizing whereas ion-neutral collisions are stabilizing. Equation (18) also demonstrates clearly the destabilizing influence of the axial electron drift u_0 (recall that $\omega_{\parallel} = k_{\parallel}u_0$).

In order to study the experimental results with a most simple model, we first use a Gaussian radial profile (12) with $N_0 = 11.75 \times 10^{15} \text{ m}^{-3}$ and $r_0 = 6.19$ cm, to approximate the (non-Gaussian) experimental profile (Fig. 2). The values of S and b have been computed with the method of [23], and the wave frequencies have been computed by solving equation (14).

The waves observed experimentally are quite regular and almost sinusoidal (Fig. 3). In the framework of a linear model, it is therefore reasonable to assume that they correspond to the fastest growing modes of the stability analysis. Using the plasma parameters given at the end of Section 3.1, we obtain the results shown in Figure 6. The drift u_0 is measured in units of the thermal electron speed

$$v_{Te} = \sqrt{\frac{KT_e}{m_e}}. \quad (19)$$

For this set of parameters the system is stable in the range $u_0 \in [0, 0.021v_{Te}]$. For larger values of u_0 , the

mode $m = 2$ is amplified and then competes with other modes. The azimuthal wavenumber of the fastest growing mode decreases with increasing axial electron drift. The fact that at fixed m , the real frequency ω_r increases when $\omega_{\parallel} = k_{\parallel}u_0$ increases, can be understood from the approximate formula (17): as soon as $u_0 \geq 0.01v_{Te}$, $\omega_{\parallel} > (1 - b/2)\omega_1$ for $m \in \{1, 2\}$. The formula (18) also shows that the strongest effect of ω_{\parallel} occurs for modes with low $b\omega_1$ and low b , i.e. modes with low m : this explains why modes with low m are preferred when u_0 increases. The results in Figure 6 show a tendency that is coherent with the experimental results of Figure 4. However the frequencies and the wavenumbers are much smaller.

The existence of a stability region at low values of u_0 depends on the plasma parameters. For instance this stability region disappears if ν_e is increased by 32%, or k_{\parallel} decreased by 13%, the other parameters being fixed. The sensitivity to the parameter r_0 , which characterizes the density profile, is stronger, since the stability region disappears if r_0 is decreased by 8% only. If the plasma parameters are varied in the confidence interval indicated in Section 3.1, whereas r_0 is varied by $\pm 8\%$, the maximal frequency of the fastest growing modes, in the range $u_0 \in [0, 0.9 v_{Te}]$, is at most 6.4 kHz, which does not fill the gap with the highest frequencies observed in the experiments, of the order of 12 kHz. This discrepancy might be due to nonlinear effects. However, we will show in the next section that a linear model taking into account the non-Gaussian experimental density profile yields fastest growing modes with properties much closer to the ones of the experimental waves.

3.3 Case of a general density profile: spectral method

Whereas solving equation (8) with a Gaussian profile is a relatively easy exercise, it is more difficult to solve (8) for an arbitrary profile. The change of variables of [23] becomes useless, Q in equation (8) depends on r in a complicated manner, i.e., $-Q$ is no more an eigenvalue of L . We present hereafter an efficient numerical technique to solve the differential equation (8).

Using a spectral approach, the solution $\phi(r)$ is expanded as follows:

$$\phi = \sum_{n=1}^N a_n f_n(r) \quad (20)$$

where N is the total number of functions f_n .

Assuming that Φ , the wave electrostatic potential, given by equation (3), is a scalar analytic function, the second corollary of the page 375 in reference [13] gives that

$$\phi = r^m \hat{\phi}(r) \quad (21)$$

with m the azimuthal wavenumber, $\hat{\phi}(r)$ an even power series of r . This implies $\hat{\phi}(0) = 0$ as soon as $m > 0$: this boundary condition, which was stated in [20], thus appears to be a regularity condition on the axis $r = 0$. On the other hand, the boundary condition (10) still holds.

Our first choice for $f_n(r)$ was $r^m(a^2 - r^2)r^{2(n-1)}$, but this choice yields badly conditioned matrices. When Chebyshev polynomials of the first kind $T_{2(n-1)}(r/a)$ are chosen the functions

$$f_n(r) = r^m(a^2 - r^2)T_{2(n-1)}(r/a) \quad (22)$$

and rather good conditioning properties are obtained.

Hence equation (8) reads

$$\sum_{n=1}^N a_n L f_n(r) = - \sum_{n=1}^N a_n Q(r) f_n(r), \quad \forall r \in [0, a]. \quad (23)$$

For the discretization in r we use collocation points defined by the N zeros of the Chebyshev polynomial $T_{2N}(r/a)$, that sit in the interval $]0, a[$, i.e.

$$r_k = a \cos \left(\frac{(2k-1)\pi}{4N} \right) \quad (24)$$

for $k \in \{1, \dots, N\}$. If we make an analogy with an interpolation problem, since $T_{2N}(r/a)$ is the first function not included in the truncated sum (20), this choice would permit to minimize the truncation error.

Equation (23) evaluated at these collocation points yields the matrix problem

$$M_L V = -M_Q V \quad (25)$$

where $V = \begin{pmatrix} a_1 \\ \vdots \\ a_N \end{pmatrix}$ is the vector representing the solution,

$$(M_L)_{kn} = L(r_k) f_n(r_k), \quad (26)$$

$$(M_Q)_{kn} = Q(r_k) f_n(r_k), \quad (27)$$

with $k, n \in \{1, \dots, N\}$.

Next we scan the (ω_r, ω_i) plane, searching for values of ω such that one eigenvalue of the matrix $M = M_L + M_Q$ vanishes within machine precision. For this purpose a method that finds the minimum of a scalar function of several variables, starting at an initial state, and uses the simplex search method [24], is used. Among these solutions one finds the couple (ω_r, ω_i) for which the instability growth rate ω_i is maximum.

In order to validate the spectral method we first consider the simpler case of a Gaussian profile (12). In this case M_Q is proportional to the scalar Q , hence Q can be found straightforwardly as the opposite of an eigenvalue. The test is performed using the parameters given by Ellis et al. in references [19,20]. The results of our spectral method totally agree with those obtained by a Runge-Kutta shooting method in figures 3a and 6a of reference [20]. However for azimuthally homogeneous modes $m = 0$, the condition $\phi(0) = 0$ is no more valid, thus the shooting method of [20] would give unphysical results, if any. On the contrary our spectral method also works for $m = 0$, and we checked that the corresponding modes are always damped.

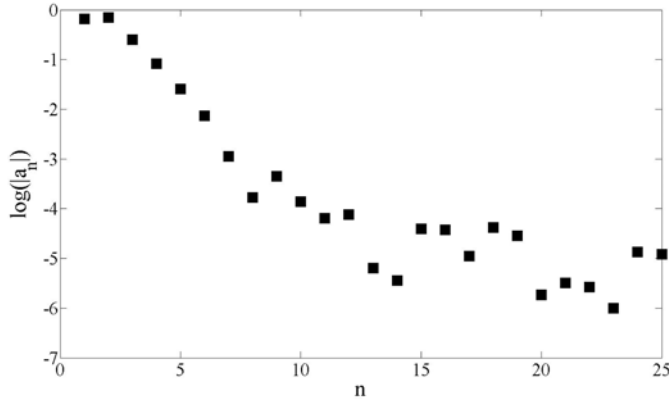


Fig. 7. With the interpolated density profile, $m = 1$, $u_0 = 0.6 v_{Te}$, decimal logarithms of coefficients a_n vs. n , for a computation with a total number of radial modes $N = 25$.

Another test is performed with our experimental parameters and the approximated Gaussian profile used in Section 3.2. With the spectral method, we recover the results of Figure 6, which were obtained by using Chen's change of variables, and an hypergeometric function.

These comparisons prove that the spectral method is capable of reliably predicting instability growth rates and perturbation profiles. Moreover, this method is much faster than the shooting one and can be used for any arbitrary density profile, contrarily to the method relying on hypergeometric functions.

3.4 Non-Gaussian density profile: results and comparison with experiments

We apply the spectral method to the experimental profile (Fig. 2), which is approximated by:

- a parabolic function between 0 and 3.3 cm,

$$n_0(r) = 11.0 \times 10^{15} - 1.34 \times 10^{18} r^2, \quad (28)$$

- a straight line between 3.3 and 7.5 cm,

$$n_0(r) = 15.65 \times 10^{15} - 1.85 \times 10^{17} r, \quad (29)$$

- a Gaussian between 7.5 cm and a ,

$$n_0(r) = 8.84 \times 10^{16} \exp(-r^2/0.038^2). \quad (30)$$

Figure 2 displays both experimental and interpolated equilibrium density profiles.

With the plasma parameters given at the end of Section 3.1, we obtain the results of Figure 7 for the coefficients a_n versus n , in the typical case $m = 1$ and $u_0 = 0.6 v_{Te}$. A spectral convergence is observed, with $|a_n| \leq A \exp(-an)$ for $2 \leq n \leq 8$, before numerical noise levels are reached. Note also that $|a_n/a_1| < 10^{-3}$ for $n > 7$. With the same parameters the fast convergence is confirmed in Figure 8 where the real frequency ω_r reaches a constant level as soon as $N \geq 6$. The same convergence is observed for the instability growth rate ω_i . Hereafter $N = 7$ will be used.

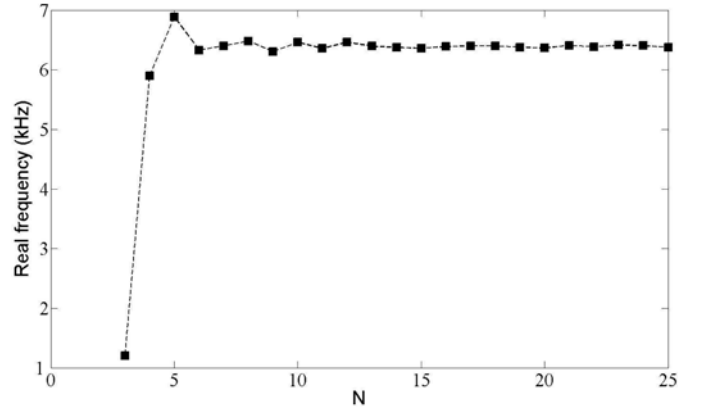


Fig. 8. In the case of Figure 7, real frequency $\omega_r/(2\pi)$ vs. the number of coefficients N .

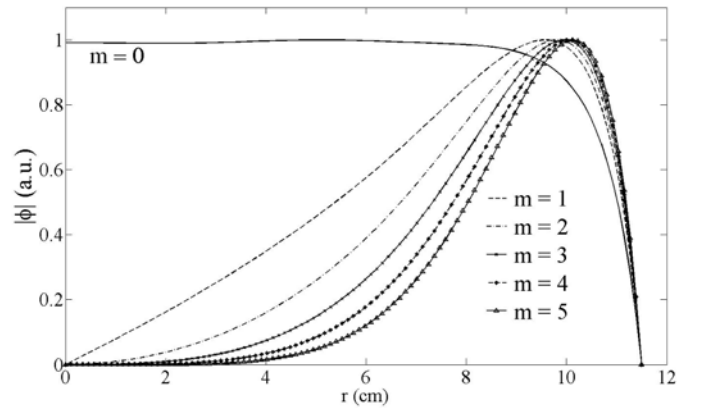


Fig. 9. With the interpolated density profile, radial profile of the modulus of the wave plasma potential for $m = 5$ to $m = 1$, for $u_0 = 0.05, 0.1, 0.15, 0.3$ to 0.6 in v_{Te} unit. The profile of the damped mode $m = 0$ is also displayed, which has been computed for $u_0 = 0.05 v_{Te}$.

Figure 9 displays the radial profile of the modulus of the wave plasma potential for $m = 1$ to $m = 5$. The profiles correspond to the fastest growing modes observed with different values $u_0 = [0.05, 0.1, 0.15, 0.3, 0.6] \times v_{Te}$. The profile of the damped mode $m = 0$ is also displayed. The fact that there is no condition like $\phi(0) = 0$ for $m = 0$ is obvious. The modes with $m > 0$ present a maximum at values of r close to a . Indeed, we noticed that in our experiment the maximum of the fluctuations is well located at the outside of the vessel.

Next Figure 10 displays the imaginary parts ω_i of the eigenfrequencies versus u_0 for different values of the azimuthal mode number m . The destabilizing influence of u_0 is clear, since for each value of m , ω_i increases when u_0 increases. Contrarily to the case of a Gaussian profile, there is no stability region for the system: some modes with $m > 5$ are amplified for u_0 close to zero. However, as soon as $u_0 > 0.05 v_{Te}$, the fastest growing modes correspond to $m \leq 5$.

Considering like in Section 3.2 the fastest growing modes, we show calculations of the corresponding real frequency versus u_0 (Fig. 11) and versus m (Fig. 12) for the

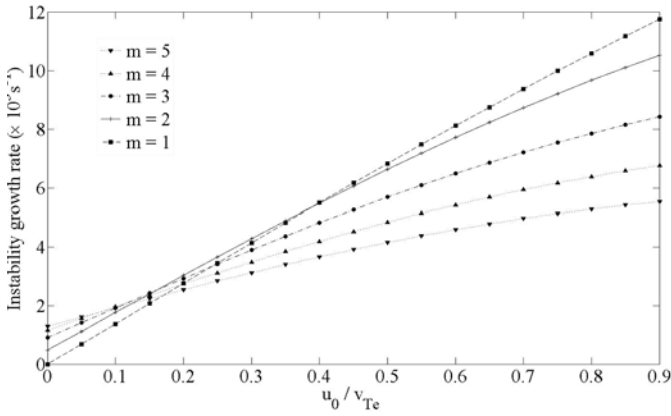


Fig. 10. With the interpolated density profile, numerical instability growth rate ω_i vs. axial electron drift u_0 .

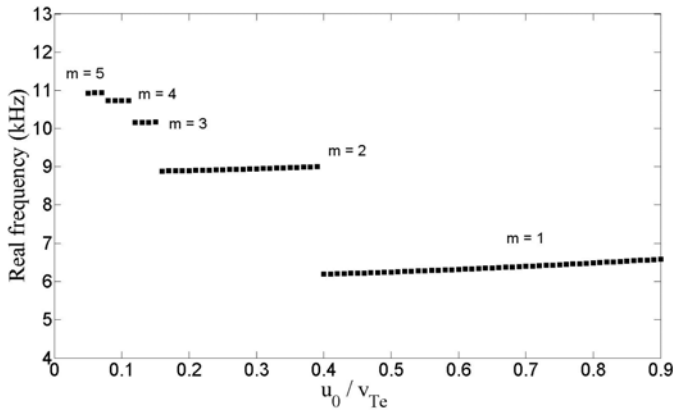


Fig. 11. With the interpolated density profile, numerical real frequencies $\omega_r/(2\pi)$ of the fastest growing mode vs. axial electron drift u_0 .

interpolated experimental profile (Fig. 2). The model predicts a decrease of the real frequency and of the mode number m when the drift u_0 increases (Fig. 11). Meanwhile, for a mode m the frequency increases until the mode suddenly changes for a lower mode with a lower frequency. Low mode frequencies depend linearly on the mode whereas for $m = 4$ and $m = 5$ the frequency reaches a plateau as it has been experimentally observed (Fig. 12).

This scenario, in the interval $u_0 \in [0.05, 0.9]v_{Te}$, is robust against changes in the plasma parameters. If we vary T_e , ν_e , B or k_{\parallel} in the confidence intervals described at the end of Section 3.1, we always find the same scenario involving the modes $m = 5$ down to $m = 1$. Referring to Figure 11, the locations of the cross-over points between two neighbouring values of m change, both in abscissa (u_0) and ordinate ($\omega_r/2\pi$), of at most 20% with respect to the values obtained with the standard parameters.

Comparing Figures 4, 11, 5 and 12, we observe that a semi-quantitative agreement is obtained between the experiments and the model, provided that we assume a linear relation between U_t and u_0 , $U_t = 1$ V corresponding to $u_0 = 0.1v_{Te}$. This strong correlation between the polarization of the tube and the electron parallel speed will be discussed hereafter.

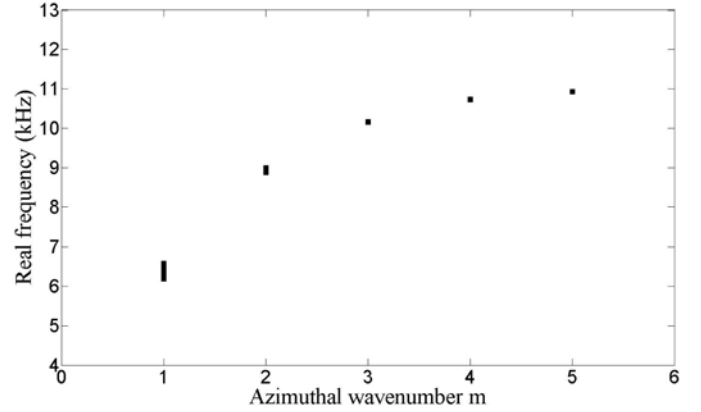


Fig. 12. Numerical real frequencies vs. the azimuthal wavenumber m .

4 Concluding discussion

The main result of this work is the bifurcation scenario observed experimentally as a function of the biasing of the confining tube U_t , or numerically as a function of the electron speed u_0 along the axis of the cylinder. The azimuthal wavenumber m of the drift waves observed in the experiments decreases when U_t increases; similarly the wavenumber m of the fastest growing mode computed theoretically decreases when u_0 increases. These variations are correlated with the decrease of the frequency as m decreases. The experimental results are in semi-quantitative agreement with the results given by the two-fluid model, provided that a non-Gaussian density profile, which interpolates closely the experimental one, is used, and that a monotonous relation between U_t and u_0 is assumed. Indeed, the stability properties of the Gaussian and non-Gaussian density profiles are quite different (compare Figs. 6 and 11). This sensitivity to the density profile has been also observed experimentally. Indeed, a small change on the experimental density profile due to a different bias of the grid for instance leads to a very different scenario. Some remaining discrepancies may be due to nonlinear phenomena, which are clearly present in the experiments, and are not considered in our model.

The link between U_t and u_0 can be analyzed as a two step process. First, it is natural to assume that the potential of the tube has a strong influence because at one axial boundary the second source chamber, not used in the experiment, is floating. This hypothesis is confirmed by some experiments where the tube potential has been modulated, which have shown a corresponding modulation of the floating potential inside the plasma, at $r = 7$ cm, with the same frequency. Denoting with U_p the value of this potential, one can assume that an increase of the tube potential U_t results in an increase of U_p . Moreover, a study of the sheath where the plasma potential varies rapidly, close to the tube, based on the model of [25], can be performed. This model can be used in the case where the magnetic field lines are not exactly parallel to the wall and here a very small angle has been assumed, which is often in agreement with real experiments. The model gives a thickness

of the Debye sheath of the order of 3 mm in the Mirabelle device. The length of this Debye sheath does not depend of U_t and can be neglected when compared to the radius of the device (11.5 cm): this confirms that it is reasonable to consider that the plasma potential is always flat except in a thin layer close to the tube. This also explains why we did not include the $E \times B$ drift in the model.

Second, as the difference $U_g - U_p > 0$ becomes smaller, the electrons encounter an electric field that increases their parallel speed. It appears therefore that increasing the potential of the tube increases the electron drift velocity.

The model has been solved numerically with a new spectral method. This spectral method is accurate and suitable for numerical investigation of drift waves in cylindrical geometry. An interesting question will be to address the transition between drift waves and ion temperature gradient instabilities using this spectral method, for a kinetic model that will allow one to take into account ion temperature gradient instability. This transition will be the object of a forthcoming paper and will complete a previous work performed with a local model [26].

The setup of the spectral method has been performed during the M1 project of A. Gaire and Q. Morel at *École des Mines de Nancy*, Department Energy: Production, Transformation.

References

1. W. Horton, Rev. Mod. Phys. **71**, 735 (1999)
2. X. Garbet, Plasma Phys. Control. Fusion **43**, A251 (2001)
3. H.W. Hendel, T.K. Chu, P.A. Politzer, Phys. Fluids **11**, 2426 (1968)
4. T.C. Simonen, T.K. Chu, H.W. Hendel, Phys. Rev. Lett. **23**, 568 (1969)
5. T. Pierre, G. Leclert, F. Braun, Rev. Sci. Instrum. **58**, 6 (1987)
6. E. Gravier, X. Caron, G. Bonhomme, T. Pierre, J.L. Briançon, Eur. Phys. J. D **8**, 451 (2000)
7. M. Matsukuma, T. Pierre, A. Escarguel, D. Guyomarc'h, G. Leclert, F. Brochard, E. Gravier, Y. Kawai, Phys. Lett. A **314**, 163 (2003)
8. O. Grulke, T. Klinger, A. Piel, Phys. Plasmas **6**, 788 (1999)
9. E. Wallace, E. Thomas, A. Eadon, J. Jackson, Rev. Sci. Instrum. **75**, 5160 (2004)
10. A.M. DuBois, A.C. Eadon, E. Thomas, Phys. Plasmas **19**, 072102 (2012)
11. R. Scarmozzino, A.K. Sen, G.A. Navratil, Phys. Rev. Lett. **57**, 1729 (1986)
12. R.G. Greaves, J. Chen, A.K. Sen, Plasma Phys. Control. Fusion **34**, 1253 (1992)
13. V.G. Pryimak, T. Miyazaki, J. Comput. Phys. **142**, 370 (1998)
14. E. Gravier, F. Brochard, G. Bonhomme, T. Pierre, J.L. Briançon, Phys. Plasmas **11**, 529 (2004)
15. T. Klinger, A. Latten, A. Piel, G. Bonhomme, T. Pierre, Plasma Phys. Control. Fusion **39**, B145 (1997)
16. T. Klinger, A. Latten, A. Piel, G. Bonhomme, T. Pierre, T. Dudok de Wit, Phys. Rev. Lett. **79**, 3913 (1997)
17. C. Schröder, O. Grulke, T. Klinger, Phys. Plasmas **9**, 4249 (2004)
18. S.A. Self, J. Plasma Phys. **4**, 693 (1970)
19. R.F. Ellis, E. Marden-Marshall, Phys. Fluids **22**, 2137 (1979)
20. R.F. Ellis, E. Marden-Marshall, R. Majeski, Plasma Phys. **22**, 113 (1980)
21. P. Baille, J.S. Chang, A. Claude, R.M. Hobson, G.L. Ogram, A.W. Yau, J. Phys. B **14**, 1485 (1981)
22. R.L. Merlino, IEEE Trans. Plasma Sci. **25**, 60 (1997)
23. F.F. Chen, Phys. Fluids **9**, 965 (1966)
24. J.C. Lagarias, J.A. Reeds, M.H. Wright, P.E. Wright, SIAM J. Opt. **9**, 112 (1998)
25. X. Zou, J.Y. Liu, Y. Gong, Z.X. Wang, Y. Liu, X.G. Wang, Vacuum **73**, 681 (2004)
26. E. Gravier, R. Klein, P. Morel, N. Besse, P. Bertrand, Phys. Plasmas **15**, 122103 (2008)